Heliyon 10 (2024) e23916

Contents lists available at ScienceDirect

Heliyon

journal homepage: www.cell.com/heliyon

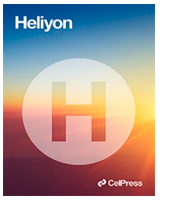

Leveraging multimodal MRI-based radiomics analysis with diverse machine learning models to evaluate lymphovascular invasion in clinically node-negative breast cancer

Yihong Jiang [a,1], Ying Zeng [a,1], Zhichao Zuo [b,1], Xiuqi Yang [a], Haibo Liu [a], Yingjun Zhou [a], Xiaohong Fan [b,*]

[a] Department of Radiology, Xiangtan Central Hospital, Xiangtan, Hunan, 411100, China
[b] The School of Mathematics and Computational Science, Xiangtan University, Xiangtan, Hunan, 411105, China

ARTICLE INFO

Keywords:
Multimodal magentic resonance imaging
Machine learning
Radiomics
Lymphovascular invasion
Clinically node-negative breast cancer

ABSTRACT

Objective: This study aimed to investigate and validate the effectiveness of diverse radiomics models for preoperatively differentiating lymphovascular invasion (LVI) in clinically node-negative breast cancer (BC).

Methods: This study included 198 patients diagnosed with clinically node-negative bc and pathologically confirmed LVI status from January 2018–July 2023. The training dataset consisted of 138 patients, while the validation dataset included 60. Radiomics features were extracted from multimodal magnetic resonance imaging obtained from T1WI, T2WI, DCE, DWI, and ADC sequences. Dimensionality reduction and feature selection techniques were applied to the extracted features. Subsequently, machine learning approaches, including logistic regression, support vector machine, classification and regression trees, k-nearest neighbors, and gradient boosting machine models (GBM), were constructed using the radiomics features. The best-performing radiomic model was selected based on its performance using the confusion matrix. Univariate and multivariable logistic regression analyses were conducted to identify variables for developing a clinical-radiological (Clin-Rad) model. Finally, a combined model incorporating both radiomics and clinical-radiological model features was created.

Results: A total of 6195 radiomic features were extracted from multimodal magnetic resonance imaging. After applying dimensionality reduction and feature selection, seven valuable radiomics features were identified. Among the radiomics models, the GBM model demonstrated superior predictive efficiency and robustness, achieving area under the curve values (AUC) of 0.881 (0.823,0.940) and 0.820 (0.693,0.947) in the training and validation datasets, respectively. The Clin-Rad model was developed based on the peritumoral edema and DWI rim sign. In the training dataset, it achieved an AUC of 0.767 (0.681, 0.854), while in the validation dataset, it achieved an AUC of 0.734 (0.555–0.913). The combined model, which incorporated radiomics and the Clin-Rad model, showed the highest discriminatory capability. In the training dataset, it had an AUC value of 0.936 (0.892, 0.981), and in the validation dataset, it had an AUC value of 0.876 (0.757, 0.995). Additionally, decision curve analysis of the combined model revealed its optimal clinical efficacy.

* Corresponding author.
E-mail address: fanxiaohong@smail.xtu.edu.cn (X. Fan).
[1] These authors contributed equally to this manuscript.

https://doi.org/10.1016/j.heliyon.2023.e23916
Received 27 September 2023; Received in revised form 12 December 2023; Accepted 15 December 2023
Available online 18 December 2023

Conclusion: The combined model, integrating radiomics and clinical-radiological features, exhibited excellent performance in distinguishing LVI status. This non-invasive and efficient approach holds promise for aiding clinical decision-making in the context of clinically node-negative BC.

1. Introduction

Metastasis is a leading cause of breast cancer (BC) recurrence, treatment failure, and tumor-related deaths. Even in patients with clinically node-negative BC, approximately 25–33 % of cases experience axillary lymph node involvement following a sentinel lymph node biopsy [1,2]. Lymphovascular invasion (LVI) plays a crucial role in lymph node involvement and is considered a potential biomarker for chemoresistance during neoadjuvant chemotherapy [1–3]. Moreover, LVI influences surgical interventions and helps determine optimal resection margins [4]. However, identifying LVI preoperatively remains challenging in clinical practice, despite the recommended preoperative determination to provide individualized and precise treatment for BC patients. Thus, early prediction of LVI should be further explored to establish reliable techniques for its accurate detection in patients with invasive BC.

Furthermore, magnetic resonance imaging (MRI) offers high spatial resolution and enables comprehensive characterization of the entire BC lesion through multimodal imaging, and its role in assessing LVI in BC is increasingly being studied. For example, previous reports have associated various clinical-radiological (Clin-Rad) features with LVI, including older age, peritumoral edema, adjacent vessel sign, diffusion-weighted imaging (DWI) rim sign, kinetic enhancement curve, and peritumor/tumor apparent diffusion coefficient (ADC) [5–8]. However, the accuracy and reliability of these features in distinguishing LVI status can sometimes be uncertain, as they mainly rely on physicians' expertise.

Moreover, radiomics has emerged as a promising field, offering a comprehensive quantification of tumor types by extracting and analyzing numerous image features [9]. Several applications of radiomics analysis in assessing LVI using advanced algorithms and artificial intelligence have been reported [10–13]. Achieving successful radiomics outcomes requires the development of reliable, highly accurate, and efficient predictive models. Therefore, it is crucial to compare different machine learning models based on radiomics-derived clinical biomarkers [14]. However, to the best of our knowledge, there has been no studies investigating the use of various radiomics-based models for distinguishing LVI status. Therefore, this study aimed to develop and validate a multimodal MRI-based combined model of radiomics and Clin-Rad features using different machine learning approaches to distinguish LVI status accurately.

2. Materials and methods

2.1. Patient population

This retrospective study was conducted from January 2018 to July 2023 and was approved by the Ethical Review Board of Xiangtan Central Hospital (No. 2022-09-004). Informed consent was waived due to the study's retrospective design.

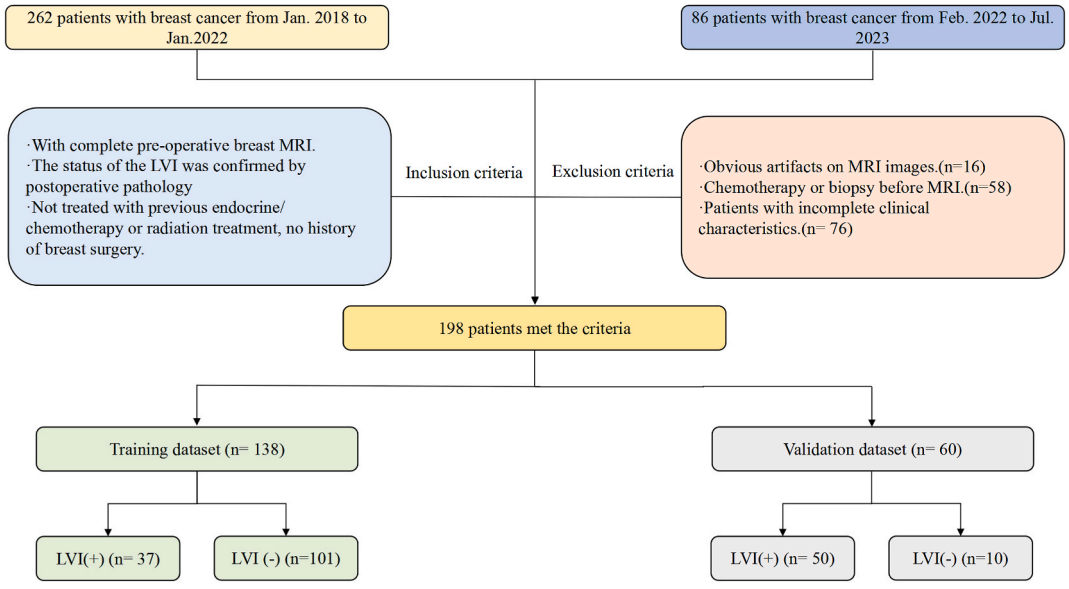

Fig. 1. Flowchart illustrating the patient enrollment process for the study.

This study included 384 patients diagnosed with clinically node-negative BC who underwent either modified radical mastectomy or breast-conserving surgery at our hospital between January 2018 and July 2023, with the study period divided into two datasets: a training dataset consisting of patients treated from January 2018–January 2022, and a validation dataset consisting of patients treated from February 2022–July 2023.

2.2. Inclusion and exclusion criteria

We included patients who have met the following inclusion criteria: i) had visible primary breast lesions on MRI, ii) were newly diagnosed with BC and underwent potentially curative surgery, and iii) underwent surgery within 2 weeks after undergoing MRI scans. We excluded patients meeting any of the following exclusion criteria: i) had previously undergone a biopsy of the breast lesion before the MRI scans, ii) had received neoadjuvant chemotherapy preoperatively, or iii) had MRI of insufficient quality, limiting the feasibility of manual segmentation. Fig. 1 shows a flowchart depicting the patient inclusion process.

2.3. MRI examination

First, patients underwent axial fat-suppressed T2-weighted imaging (T2WI), axial non-fat T1-weighted imaging (T1WI), diffusion-weighted imaging (DWI), apparent diffusion coefficient (ADC), and dynamic contrast-enhanced MRI (DCE-MRI) in the prone position. The imaging was then performed using a 1.5-T MAGNETOM Aera MRI scanner (Siemens Healthcare, Erlangen, Germany) with an 18-channel surface breast coil. Next, the imaging protocol comprised axial fat-suppressed T2WI (inversion time, 165 ms; TR/TE, 4830/48; flip angle, 170°; field of view [FOV], 340–340 mm; acquisition matrix [Acq], 336 × 448; average, 2; slice thickness, 4 mm); axial T1WI (TR/TE, 8.08/4.77; flip angle, 20°; FOV, 320–320 mm; Acq, 336 × 448; average, 1; slice thickness, 1.1 mm); DWI with b-values of 0 and 1000 s/mm2 (TR/TE, 7460/66; FOV, 153–340 mm; Acq, 72 × 160; slice thickness, 5 mm); and DCE-MRI (TR/TE, 5.03/2.39; flip angle, 10°; FOV, 360–360 mm; Acq, 218 × 256; average, 1; slice thickness, 1.6 mm). Gadoteric acid meglumine salt, a contrast agent, was injected at a rate of 3 mL/s through a high-pressure injector at a dose of 0.2 mL/kg. After acquiring pre-contrast images, the contrast agent was administered, and flushed by a 20-mL isotonic sodium chloride solution injection. Finally, six consecutive scans of 90 s each were performed.

2.4. Histopathological examination

The excised tumor samples were immersed in 10 % formalin, then embedded in paraffin and sliced into 4-μm-thick sections. These sections were later stained with hematoxylin and eosin. To assess LVI, the resected tissue samples were examined under a microscope, with special focus on locating tumor cells within the vascular spaces. LVI refers to the presence of tumor cells within lymphatic or blood vessels, and its accurate identification and characterization require thorough histopathological analysis conducted by experienced pathologists.

2.5. MR image analysis

The MR images were evaluated using monitors integrated into a picture archiving and communication system (PACS). All images

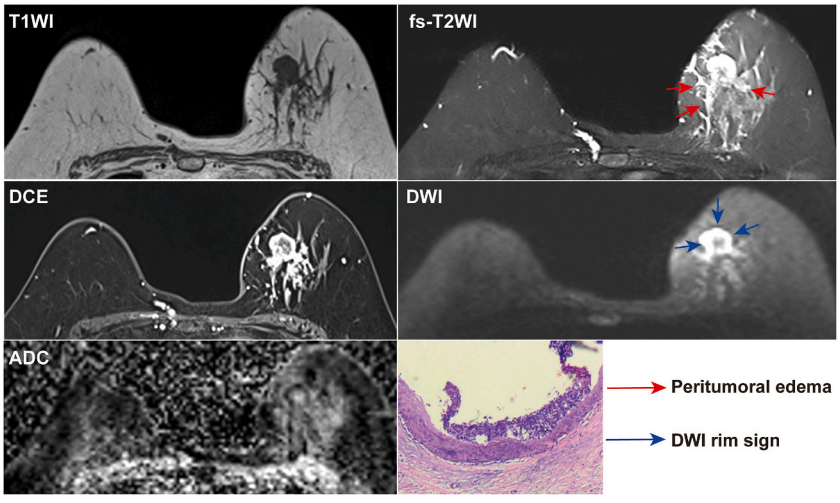

Fig. 2. The patient is a 49-year-old female diagnosed with invasive breast cancer and lymphovascular invasion. Preoperative multimodal MRI (T1WI, fs-T2WI, DCE, DWI, ADC) was performed, revealing typical MR morphological features: peritumoral edema (indicated by the red arrows) and DWI rim sign (indicated by the blue arrows).

were anonymized, randomized, and independently assessed by two experienced radiologists specializing in breast MRI interpretation. Discrepancies were resolved through consensus discussions. Radiologists based their interpretations on specific conventional features observed in the findings of MRI.

Moreover, peritumoral edema was visually assessed on fat-suppressed T2WI, where hyperintensity surrounding the tumor mass indicated its presence [5]. Fat-suppressed T2WI were also used to evaluate subcutaneous edema, skin thickening, or high signal intensity within the subcutaneous tissue [6]. In addition, intratumoral high signal intensity was identified as signal intensity greater than that of the surrounding breast tissue on fat-suppressed T2W images [6]. The DWI rim sign was defined as a hyperintense rim visible on DWI, outlining either $\geq$90 % of the lesion (complete) or <90 % (incomplete) [7]. adjacent vessel sign determination involved examining vessels entering the enhanced lesion or in contact with its edge [6], while increased ipsilateral vascularity as a higher number of vessels within the breast affected by cancer compared to the contralateral breast, with a difference of one or more vessels [6]. Internal enhancement patterns were classified into three categories: homogeneous, heterogeneous, or exhibiting rim enhancement [7]. Fig. 2 presents the characteristic morphological features of a typical MR image alongside a pathological image depicting the presence of LVI.

2.6. Image segmentation and radiomic feature extraction

First, the T2WI, DCE, DWI, and ADC maps of all patients were obtained from PACS. These images underwent preprocessing to standardize the gray-level intensity ranges and were resampled to a voxel size of $1 \times 1 \times 1$ mm^3, following which they were imported into the open-source software, three-dimensional (3D) Slicer (version 4.6; https://www.slicer.org). This software is commonly used for medical image informatics, processing, and 3D visualization [15].

Initially, a radiologist with 5 years of experience in MRI of breast lesions manually and volumetrically delineated the region of interest (ROI). Subsequently, another radiologist with 10 years of experience in the same field reviewed and adjusted the lesion delineation accordingly.

ROI delineation followed specific guidelines, which included aligning five modal images (T1WI, T2WI, DCE, DWI, and ADC) through image registration. For this purpose, we used the 3D Slicer software, specifically the Elastix module. The Elastix module offers different preset registration methods. In this study, we utilized the 3D DCE-MRI (breast) method, which is designed for breast analysis. By applying a registration algorithm with a selected set of parameters, we accurately aligned the phase I image, which had the highest intensity in the DCE images, with the anatomical features and positioning of the other modal images. After the alignment, we delineated the ROIs along the tumor margin. To generate a mask representing the entire tumor, we utilized the phase I image and transferred it to the other modal images.

2.7. Radiomics feature dimensionality reduction and selection

The Pyradiomics function package (https://pyradiomics.readthedocs.io) was utilized to extract radiomic features from DCE, T2WI, DWI, and ADC maps [16]. The process involved three main steps. First, a Z-score transformation method was applied to standardize the scale of each radiomics feature, reducing dimensional heterogeneity caused by varying values. Next, the minimum redundancy–maximum correlation (mRMR) approach was used to select the most relevant tumor classification features while minimizing redundancy. For the feature selection phase, the LASSO regression model with 10-fold cross-validation (CV) was employed to identify features with non-zero coefficients. These procedures were then carried out on the training dataset and subsequently applied to the validation dataset. Fig. 3 shows the radiomics process, showcasing ROI delineation, feature extraction, dimensionality reduction, and

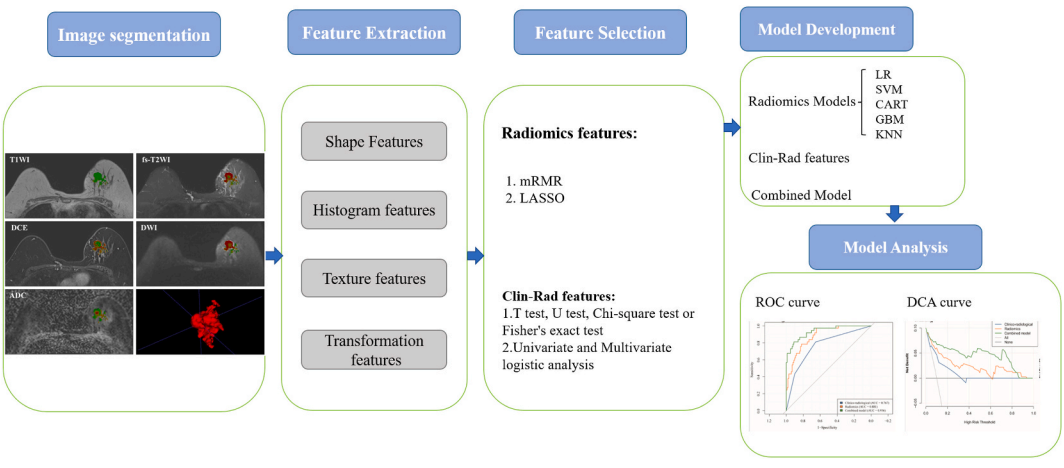

Fig. 3. Visual representation of the radiomics process, depicting ROI delineation, feature extraction, dimensionality reduction, and feature selection.

feature selection.

2.8. Development of radiomics signature models

After conducting feature dimensionality selection using LASSO regression, the radiomic features were further refined using machine learning. The final selection of radiomic features was then used to build robust radiomics models with the goal of identifying a classifier that has exceptional recognition capabilities within the provided dataset. In present study, we considered five prominent training models: logistic regression (LR), support vector machine (SVM), classification and regression trees (CART), k-nearest neighbors (KNN), and gradient boosting machine (GBM).

The "caret" R package was used in this study to explain five machine learning approaches. During the model training process, a control object was defined with 10-fold CV, the summaryFunction was set to "twoClassSummary," allowing retrieval of predicted probabilities for different models. The LR, SVM, CART, KNN, and GBM were trained using the corresponding functions "glm," "svmLinear," "rpart," "knn," and "gbm," respectively. We compared the diagnostic performance of these models using the area under

Table 1
Comparison of clin-rad features between the training and validation datasets.

Variables	Total (n = 198)	Training dataset (n = 138)	Validation dataset (n = 60)	p-value
LVI status, n (%)				0.174
LVI(−)	151 (76.3)	101 (73.2)	50 (83.3)	
LVI(+)	47 (23.7)	37 (26.8)	10 (16.7)	
Age, Median (Q1,Q3)	51 (45, 57.8)	51 (45, 58)	50 (44, 56.2)	0.434
Menopausal status, n (%)				0.711
Premenopausal	100 (50.5)	68 (49.3)	32 (53.3)	
Postmenopausal	98 (49.5)	70 (50.7)	28 (46.7)	
Location, n (%)				1
Left	106 (53.5)	74 (53.6)	32 (53.3)	
Right	92 (46.5)	64 (46.4)	28 (46.7)	
TIC curves, n (%)				0.871
Type I	11 (5.6)	8 (5.8)	3 (5)	
Type II	67 (33.8)	45 (32.6)	22 (36.7)	
Type III	120 (60.6)	85 (61.6)	35 (58.3)	
FGT density, n (%)				0.77
Dense	48 (24.2)	33 (23.9)	15 (25)	
Heterogeneously dense	71 (35.9)	47 (34.1)	24 (40)	
Scattered	52 (26.3)	39 (28.3)	13 (21.7)	
Predominantly fatty	27 (13.6)	19 (13.8)	8 (13.3)	
BPE, n (%)				0.813
None/minimal	48 (24.2)	36 (26.1)	12 (20)	
Mild	83 (41.9)	56 (40.6)	27 (45)	
Moderate	43 (21.7)	29 (21)	14 (23.3)	
Marked	24 (12.1)	17 (12.3)	7 (11.7)	
Intratumoral high signal intensity, n (%)				0.296
Absence	147 (74.2)	99 (71.7)	48 (80)	
Presence	51 (25.8)	39 (28.3)	12 (20)	
Peritumoral edema, n (%)				0.469
Absence	133 (67.2)	90 (65.2)	43 (71.7)	
Presence	65 (32.8)	48 (34.8)	17 (28.3)	
Subcutaneous edema, n (%)				0.966
Absence	163 (82.3)	113 (81.9)	50 (83.3)	
Presence	35 (17.7)	25 (18.1)	10 (16.7)	
Intratumoral necrosis, n (%)				0.163
Absence	158 (79.8)	106 (76.8)	52 (86.7)	
Presence	40 (20.2)	32 (23.2)	8 (13.3)	
Internal enhancement pattern, n (%)				0.149
Homogeneous	15 (7.6)	8 (5.8)	7 (11.7)	
Heterogeneous	155 (78.3)	107 (77.5)	48 (80)	
Rim enhancement	28 (14.1)	23 (16.7)	5 (8.3)	
Adjacent vessel sign, n (%)				0.27
Absence	76 (38.4)	49 (35.5)	27 (45)	
Presence	122 (61.6)	89 (64.5)	33 (55)	
Increased ipsilateral vascularity, n (%)				0.81
Absence	108 (54.5)	74 (53.6)	34 (56.7)	
Presence	90 (45.5)	64 (46.4)	26 (43.3)	
DWI rim sign, n (%)				0.052
Absence	145 (73.2)	95 (68.8)	50 (83.3)	
Presence	53 (26.8)	43 (31.2)	10 (16.7)	

Abbreviation: Clin-Rad, Clinico-radiological; TIC, time-signal intensity; FGT, fibroglandular tissue; BPE, breast parenchymal enhancement; DWI, diffusion weighted imaging; LVI, lymphovascular invasion.

the curve (AUC) derived from the receiver operating characteristic curve (ROC), as well as sensitivity and specificity measures. Subsequently, we conducted a screening process to determine the most effective radiomics model.

2.9. Clin-Rad and combined models' construction

First, univariate logistic regression analysis on predictor variables that included clinical and radiological characteristics from the training dataset were performed. Next, we conducted multivariable logistic regression using a p-value <0.1 to identify the optimal predictor variables for model development. Odds ratios (ORs) and 95 % confidence intervals (CIs) were calculated for each factor. To recognize the precision, impartiality, and reliability of machine learning models in assisting clinical decision-making [14], we utilized the selected predictors to construct a combined model based on the superior radiomics model. Then, the model's performance was evaluated and validated using confusion matrix analysis on the training and validation datasets using evaluation parameters, including AUC, sensitivity, and specificity. Decision curve analysis (DCA) was employed to classify LVI status and assess the clinical effectiveness of the models, which quantified net benefits at various threshold probabilities with both the training and validation datasets.

2.10. Statistical analysis

We performed statistical analysis using R software (version 4.1.0; https://www.r-project.org). For continuous variables, the Student's t-test was used for normally distributed data, while the Mann–Whitney *U* test was used for non-normally distributed data. The chi-squared test was employed for categorical variables. $P < 0.05$ was considered statistically significant.

3. Results

3.1. Patients' population and Clin-Rad features

In total, 198 patients were enrolled, with 138 included in the training dataset and 60 in the validation dataset. No significant differences were observed between these two datasets (Table 1). Within the training dataset, significant differences were observed in several features when comparing patients with LVI (−) and LVI (+), including location, peritumoral edema, adjacent vessel sign, and DWI rim sign (see Supplementary Table 1).

We conducted univariate and multivariate logistic regression analyses to identify independent predictors of LVI (+), which indicated that peritumoral edema (OR 1.292, 95 % CI 1.109–1.504, p = 0.001) and DWI rim sign (OR 1.279, 95 % CI 1.095–1.495, p = 0.002) significantly influenced the likelihood of LVI (+) (Table 2).

3.2. Radiomic signature models and performances

A total of 1239 radiomics features were extracted from the multimodal MRI images, including T1WI, T2WI, DCE, ADC, and DWI, and 6195 radiomic features were obtained. After performing feature dimensionality reduction and selection (Figs. 4 and 5), seven features with nonzero coefficients were retained.

Figs. 6 and 7 present the ROC curves, AUC, sensitivity, and specificity of the five radiomics models (LR, SVM, KNN, CART, GBM) in the training and validation datasets. Our observations revealed that the GBM model outperformed the other models, achieving the highest AUC values in both datasets. The AUC in the training dataset was 0.881 (95 % CI 0.823–0.940), with a sensitivity of 0.973 and specificity of 0.644. Similarly, the validation dataset exhibited an AUC of 0.820 (95 % CI 0.693–0.947), with a sensitivity of 0.900 and

Table 2
Univariate and multivariable logistic regression analyses for selecting Clin-Rad features of model development.

Variants	Odd Ratio (95%CI)	p-value	Odd Ratio (95%CI)	p-value
	Univariate		Multivariate	
Age	0.99 (0.96–1)	0.54		
Menopausal status	1 (0.49–2.2)	0.93		
Location	2.1 (0.96–4.4)	0.064		
TIC curves	1.3 (0.67–2.5)	0.45		
FGT density	1.1 (0.74–1.6)	0.67		
BPE	1 (0.7–1.5)	0.88		
Intratumoral high signal intensity	1.3 (0.58–3)	0.51		
Peritumoral edema	5.9 (2.6–13)	< 0.001	1.292 (1.109–1.504)	0.001
Subcutaneous edema	1.1 (0.41–2.8)	0.88		
Intratumoral necrosis	1.1 (0.45–2.6)	0.85		
Internal enhancement pattern	1.2 (0.53–2.7)	0.68		
Adjacent vessel sign	2.5 (1–6)	0.043	1.058 (0.916–1.222)	0.442
Increased ipsilateral vascularity	0.84 (0.39–1.8)	0.66		
DWI rim sign	5.6 (2.5–13)	< 0.001	1.279 (1.095–1.495)	0.002

Abbreviation: Clin-Rad, Clinico-radiological; TIC, time-signal intensity; FGT, fibroglandular tissue; BPE, breast parenchymal enhancement; DWI, diffusion weighted imaging.

specificity of 0.680 (Table 3). Thus, the GBM model was selected as the optimal radiomic model to ensure the stability and reliability of our study.

3.3. Combined model construction and validation

A Clin-Rad model was developed by peritumoral edema and the DWI rim sign. The model achieved an AUC of 0.767 (0.681, 0.854) with a sensitivity of 0.811 and specificity of 0.653 in the training dataset. In the validation dataset, the AUC was 0.734 (0.555–0.913) with a sensitivity of 0.700 and specificity of 0.700. The Clin-Rad model was integrated with the radiomics model constructed using the optimal machine learning model (GBM) to provide a comprehensive evaluation of diagnostic efficacy.

Fig. 8 shows the ROC curves of the three models in the training and validation datasets. The combined model demonstrated considerably improved discrimination ability and provided a comprehensive evaluation compared to the Clin-Rad and radiomic models (Table 4). This improvement is indicated by higher AUC values: 0.936 (0.892, 0.981) with a sensitivity of 0.811 and specificity of 0.911 in the training dataset, and AUC values of 0.876 (0.757, 0.995) with a sensitivity of 0.900 and specificity of 0.720 in the validation dataset. In addition, Fig. 9 presents the DCAs of the three models, which further supports the superior performance of the combined model. Therefore, we believe the combined model provided the most substantial net benefit for classifying LVI status accurately.

4. Discussion

Our results suggest that integrating multimodal MRI-based radiomics models with Clin-Rad features can enhance the classification of LVI status accurately and improve comprehensive diagnostic efficacy. Therefore, we developed a combined model that integrates the predictive capabilities of Clin-Rad predictors and radiomics signatures using GBM, to achieve satisfactory classification outcomes for LVI status and offer a feasible and reliable noninvasive method for evaluating malignant behavior and treatment strategies in patients with clinically node-negative BC.

Clin-Rad model developed using peritumoral edema and DWI rim sign. Macroscopically, peritumoral edema is associated with aggressive tumor characteristics, such as large tumor size, LVI, and a high Ki-67 index, which may indicate a poor prognosis [3,6,17], and microscopically in BC to pathological features, including angiectasia, growth pattern, interstitial fibrosis, and tumor necrosis. The presence of peritumoral edema may result from mechanical obstruction of vascular and lymphatic vessels by LVI tumor emboli, leading to secondary fluid retention or leakage in the surrounding space. This incomplete neovascularization and abnormal lymphatic

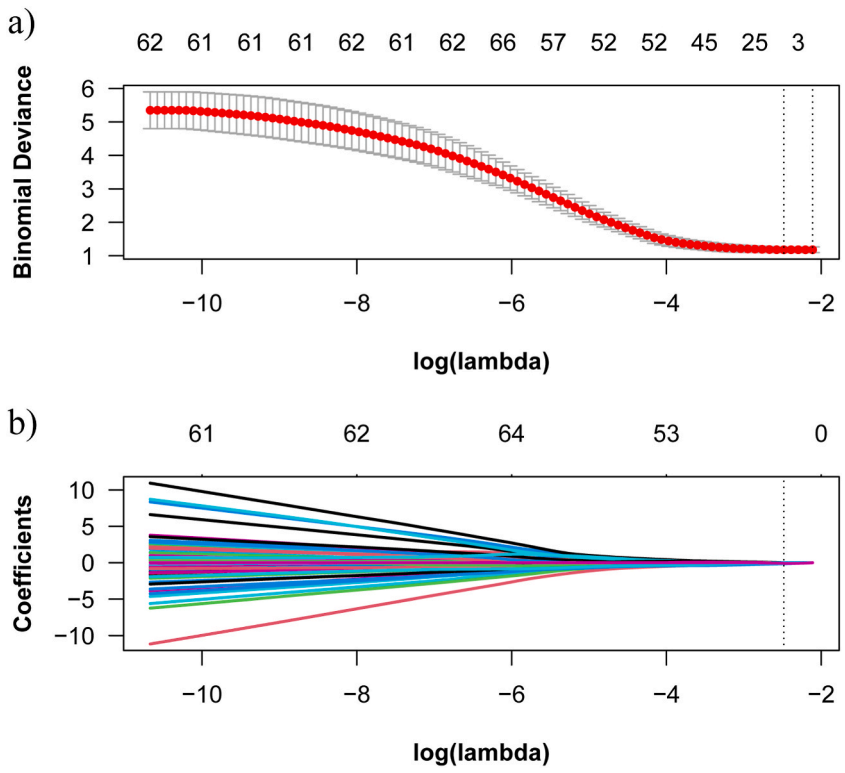

Fig. 4. (a) The LASSO regression algorithm was utilized for dimensionality reduction of radiomics features. (b) Shows the optimal parameter (λ) interval for Lasso regression using 10-fold cross-validation.

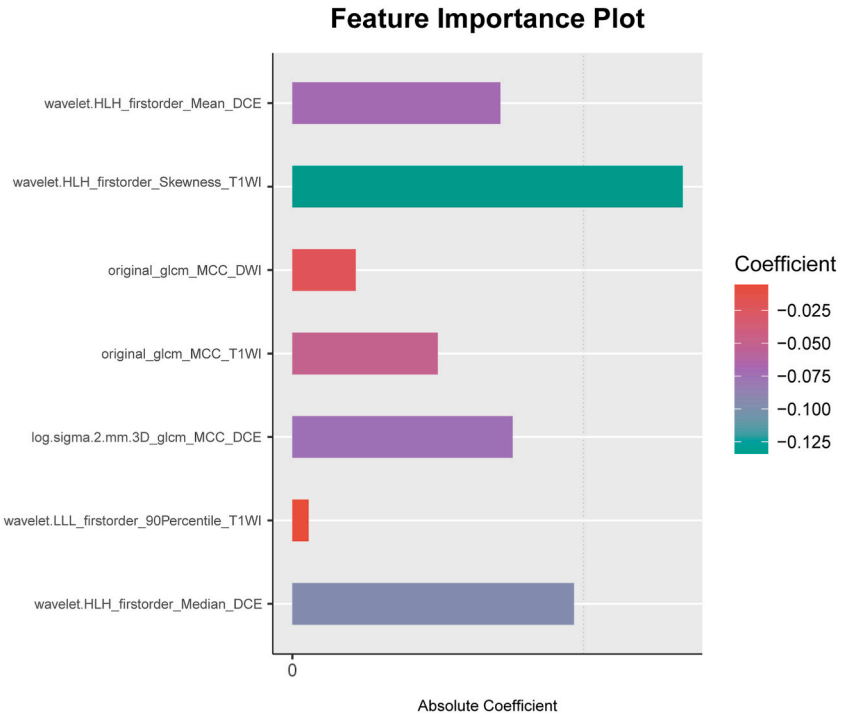

Fig. 5. Conducting feature dimensionality reduction and identifying features through the LASSO method.

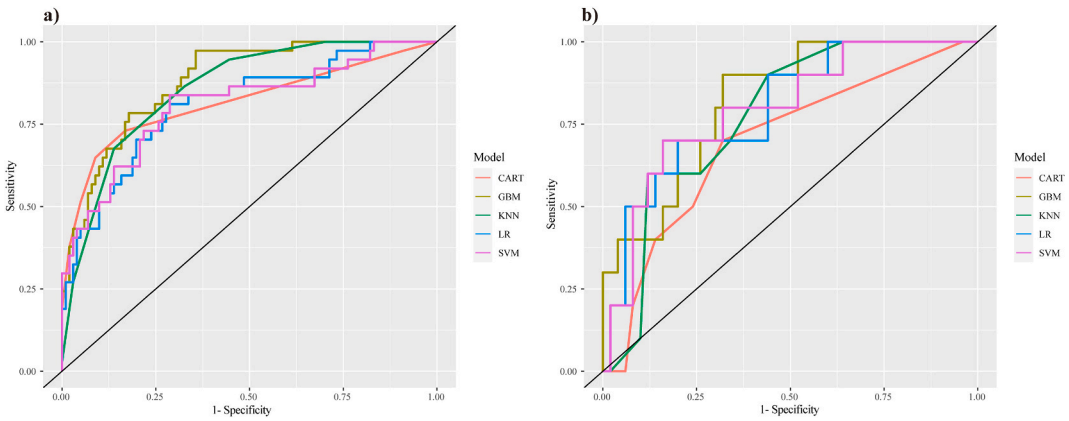

Fig. 6. Receiver operating characteristic (ROC) curves of radiomics models based on five machine learning algorithms (logistic regression [LR], support vector machine [SVM], k-nearest neighbors [KNN], classification and regression trees [CART], and gradient boosting machine [GBM]) in the training dataset (a) and validation dataset (b).

drainage causes vascular leakage and increased interstitial fluid pressure [18]. Moreover, peritumoral edema is associated with the presence of hyaluronic acid, which reflects malignant behavior. For example, an accumulation of hyaluronic acid in the stromal tissue surrounding BC leads to an increase in T2 relaxation time on MR images [19]. Furthermore, peritumoral edema has been related to high levels of tumor-infiltrating lymphocytes, which are considered a precursor to LVI [20]. The DWI rim sign is a useful indicator of malignancy in BC, and is associated with tumor histological features, such as grade, size, and subtype. Additionally, this sign demonstrates a borderline correlation with Ki-67, a protein that serves as a marker of cancer aggressiveness by reflecting the cell proliferation rate [21,22]. Furthermore, our findings align with the previous study reporting a consistent association between the DWI rim sign and LVI [7]. However, the limitations of these studies mainly arise from the subjective impact of individual clinical experience and the dependence on a single evaluation index. Currently, there is no consensus on the classification of LVI status using MRI morphological characteristics. Hence, innovative noninvasive methods for assessing LVI status should be investigated.

Radiomics is a cutting-edge, non-invasive methodology that employs intelligent algorithms to construct models based on original medical images. This methodology yields additional insights and reveals potentially pertinent phenotypic information by capturing

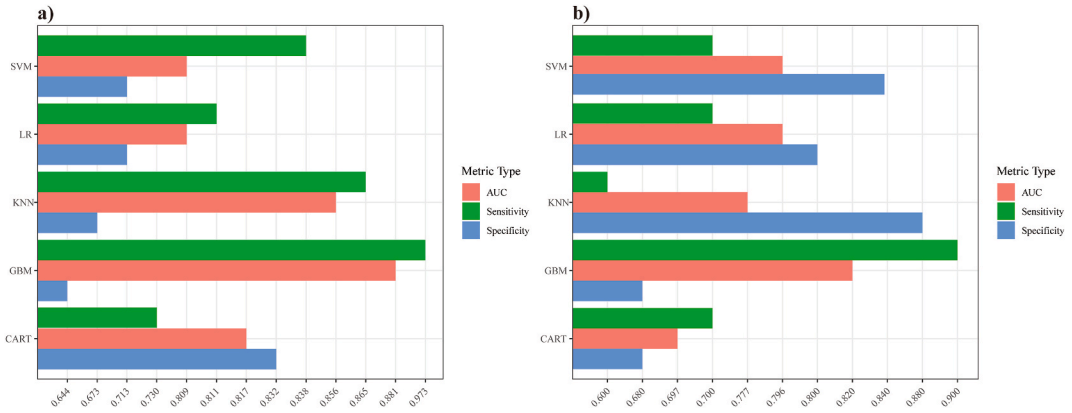

Fig. 7. The area under the curve, sensitivity, and specificity of the five radiomics models (LR, SVM, KNN, CART, GBM) in both the training dataset (a) and validation dataset (b).

Table 3
Diagnostic performance of various machine learning models in predicting LVI in clinically node-negative breast cancer.

Model	Datasets	AUC (95%CI)	Sensitivity	Specificity
SVM	Training	0.809 (0.721,0.897)	0.838	0.713
	Validation	0.796 (0.646,0.946)	0.700	0.840
CART	Training	0.817 (0.730,0.903)	0.730	0.832
	Validation	0.697 (0.528,0.866)	0.700	0.680
KNN	Training	0.856 (0.792,0.920)	0.865	0.673
	Validation	0.777 (0.644,0.910)	0.600	0.880
LR	Training	0.809 (0.725,0.893)	0.811	0.713
	Validation	0.796 (0.649,0.943)	0.700	0.800
GBM	Training	0.881 (0.823,0.940)	0.973	0.644
	Validation	0.820 (0.693,0.947)	0.900	0.680

Abbreviation: LVI, lymphovascular invasion; AUC, area under the curve; SVM, Support Vector Machine; CART, Classification and Regression Trees; KNN, K-Nearest Neighbors; LR, Logistic Regression; GBM, Gradient Boosting Machine.

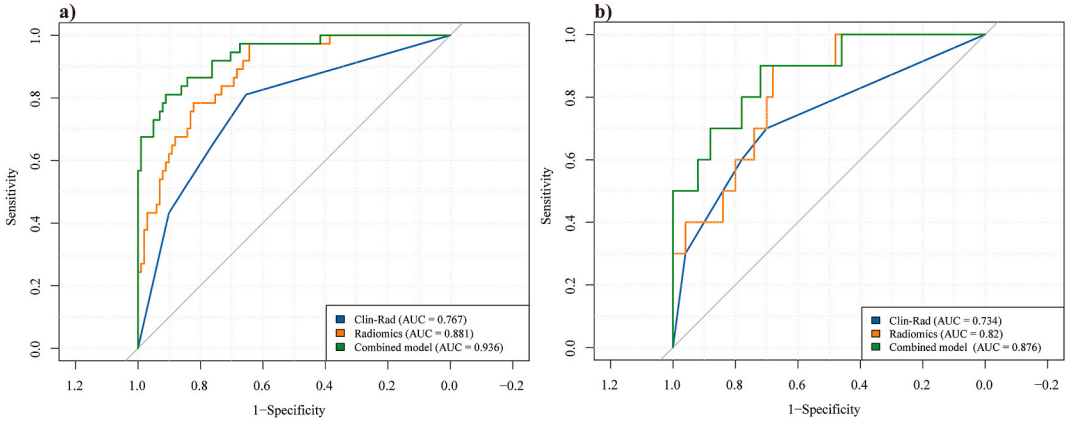

Fig. 8. Display of the ROC curves of the three models in both the training dataset (a) and validation dataset (b).

tumor heterogeneity [9]. The rationale for using multimodal MRI images for radiomics analysis is the complementary information provided by different sequences. Multimodal imaging allows for the holistic characterization of tissue properties, capturing diverse aspects like morphology, function, and the hemodynamic changes. This comprehensive approach improves the efficiency of radiomics analysis, leading to a deeper understanding of underlying biological processes and disease phenotypes. The results of our study indicated that the radiomics model developed by the GBM algorithm outperformed other machine learning models. GBM is an ensemble learning algorithm that utilizes decision trees as base models to generate a more powerful predictive model through iterative training of a series of weak classifiers. It optimizes the model using gradient descent and corrects the errors of the previous model in each iteration. This algorithm has consistently demonstrated superior performance in various applications, including classification,

Table 4
Diagnostic performance of various machine learning models in predicting LVI in clinically node-negative breast cancer.

Model	Datasets	AUC (95%CI)	Sensitivity	Specificity
Clin-Rad	Training	0.767 (0.681,0.854)	0.811	0.653
	Validation	0.734 (0.555,0.913)	0.700	0.700
Radiomics*	Training	0.881 (0.823,0.940)	0.973	0.644
	Validation	0.820 (0.693,0.947)	0.900	0.680
Combined	Training	0.936 (0.892,0.981)	0.811	0.911
	Validation	0.876 (0.757,0.995)	0.900	0.720

Abbreviation: LVI, lymphovascular invasion; AUC, area under the curve.
* Represents models were constructed using Gradient Boosting Machine (GBM).

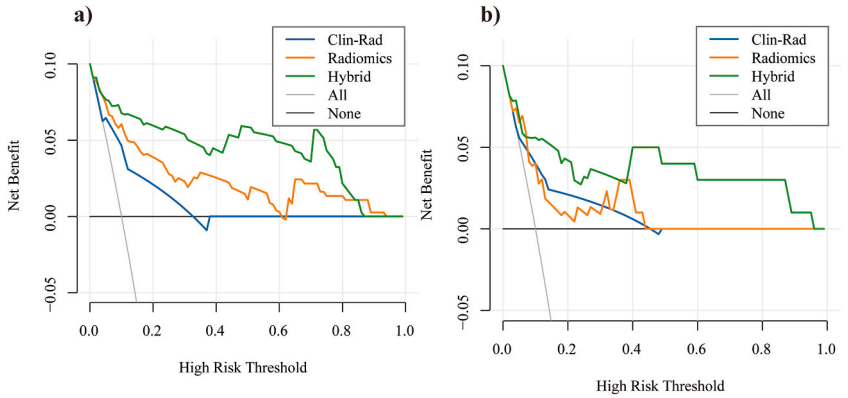

Fig. 9. Presentation of the decision curve analyses (DCAs) of the three models (Clin-Rad, radiomic models, and combined model) in both the training dataset (a) and validation dataset (b).

regression, and ranking tasks. For instance, Lee et al. [23] found that the GBM algorithm achieved better performance than LR in predicting early gastric cancer, while Zhou et al. [24] demonstrated that GBM achieved higher accuracy and AUC value than other machine learning models for predicting peritoneal metastasis of gastric cancer by combining dimensionality reduction techniques with different models. This study integrated both Clin-Rad model and radiomics model to establish a combined, which demonstrated the best and most comprehensive diagnostic performance, followed by the radiomics model and then the Clin-Rad model. BC exhibiting LVI (+), indicative of cancer aggressiveness, tend to exhibit rapid growth and increased susceptibility to necrosis and micro-hemorrhage. Thus, these factors contribute to heightened tumor heterogeneity compared to those without LVI (−). Radiomics models demonstrate superior predictive capabilities compared to Clin-Rad features, because they could quantitatively detect additional heterologous and heterogeneous features that cannot be visually interpreted. This indicates that while radiomics models outperform Clin-Rad features in terms of predictive capabilities, Clin-Rad remains a useful predictive model. Hence, the combined model accurately predicts LVI status by integrating vital information from other models. Incorporating multi-domain and abundant data into the combined model enhances the diagnostic efficiency for predicting LVI. The radiomics model, based on the GBM algorithm, demonstrates high diagnostic efficiency with an AUC of 0.881 (0.823, 0.940) in the training dataset and 0.820 (0.693, 0.947) in the validation dataset. The sensitivity is high in the training and validation datasets at 0.973 and 0.900, respectively, but the specificity remains relatively low at 0.644 and 0.680 in the training and validation datasets. However, when Clin-Rad and radiomics are combined, the constructed model achieves a higher AUC value of 0.936 (0.892, 0.981) in the training dataset and 0.876 (0.757, 0.995) in the validation dataset. This enhancement is particularly evident in specificity, which significantly improves to 0.911 and 0.720 in the training and validation datasets, respectively. Importantly, the diagnostic performance achieved by the combined model, constructed using machine learning algorithms in this study, is comparable to the study by Feng et al. [10], which uses deep learning with transfer learning to predict LVI. Specifically, this present study avoids overfitting and demonstrates a more practical and robust model.

However, this study had some limitations. First, it focused solely on analyzing intra-tumoral radiomic features while disregarding peri-tumoral radiomic features, which have been shown to hold significance in predicting LVI [25]. To enhance the comprehensiveness of future research, peritumoral radiomic signs should be included in future studies. Second, the retrospective design and limited sample size of this study restrict its generalizability. A larger-scale multicenter prospective trial should be conducted in the future to validate and reinforce these findings and ensure their applicability to a wider population. Third, integrating data from multiple imaging sequences poses challenges. Variations in acquisition parameters, image quality, and potential co-registration errors may introduce sources of variability that can confound the analysis. Additionally, the presence of artifacts and technical limitations specific to each MRI sequence may impact the reliability and reproducibility of radiomics features. Lastly, the manual delineation of regions of interest introduces the possibility of interobserver variability, which can limit the clinical utility of the findings. Therefore, future studies should employ automated or semi-automated methods for region delineation; this would increase consistency and reduce

observer-dependent variations.

5. Conclusions

Our study introduced and validated a multimodal MRI-based combined model that integrates Clin-Rad features and radiomics features for classifying LVI status. We demonstrated that the combined model, employing GBM, had the highest diagnostic performance. This study has the potential to significantly enhance clinical decision accuracy, patient prognosis, and treatment selection. Through our approach, which aligns with the principles of precision medicine, this study may contribute to revolutionize clinical therapeutic strategies and lead to tailored and more effective patient care.

Ethics approval and consent to participate

This retrospective study, conducted from January 2018 to July 2023, was approved by the Ethical Review Board of Xiangtan Central Hospital (No. 2022-09-004). The requirement for informed consent was waived by the Ethical Review Board owing to the retrospective design of the study.

Data availability statement

The processed data required to reproduce these findings were available at https://github.com/fanxiaohong/Breast-Cancer-Dataset.

Funding

This work was supported by the Postgraduate Scientific Research Innovation Project of Hunan Province (Grant no. CX20210598) and Postgraduate Scientific Research Innovation Project of Xiangtan University (Grant no. XDCX2021B097), P. R. China.

CRediT authorship contribution statement

Yihong Jiang: Writing – original draft, Software, Methodology, Formal analysis, Conceptualization. **Ying Zeng:** Methodology, Formal analysis, Conceptualization. **Zhichao Zuo:** Writing – review & editing, Software, Methodology, Conceptualization. **Xiuqi Yang:** Investigation, Formal analysis, Data curation. **Haibo Liu:** Validation, Supervision, Data curation. **Yingjun Zhou:** Validation, Supervision, Data curation. **Xiaohong Fan:** Writing – review & editing, Validation, Supervision, Methodology, Formal analysis, Conceptualization.

Declaration of competing interest

The authors declare that they have no known competing financial interests or personal relationships that could have appeared to influence the work reported in this paper.

Acknowledgements

We would like to thank Editage (www.editage.com) for English language editing.

Appendix A. Supplementary data

Supplementary data to this article can be found online at https://doi.org/10.1016/j.heliyon.2023.e23916.

References

[1] T.S. Alsumai, N. Alhazzaa, A. Alshamrani, S. Assiri, A. Alhefdhi, Factors predicting positive sentinel lymph node biopsy in clinically nodenegative breast cancer, Breast Cancer 14 (2022) 323–334.
[2] Y. Zhang, J. Li, Y. Fan, X. Li, J. Qiu, M. Zhu, H. Li, Risk factors for axillary lymph node metastases in clinical stage t1-2n0m0 breast cancer patients, Medicine 98 (40) (2019), e17481.
[3] T. Uematsu, M. Kasami, J. Watanabe, K. Takahashi, S. Yamasaki, K. Tanaka, Y. Tadokoro, A. Ogiya, Is lymphovascular invasion degree one of the important factors to predict neoadjuvant chemotherapy efficacy in breast cancer? Breast Cancer 18 (4) (2010) 309–313.
[4] Y.-M. Zhong, F. Tong, J. Shen, Lympho-vascular invasion impacts the prognosis in breast-conserving surgery: a systematic review and meta-analysis, BMC Cancer 22 (1) (2022) 102.
[5] H. Cheon, H.J. Kim, T.H. Kim, H.-K. Ryeom, J. Lee, G.C. Kim, J.-S. Yuk, W.H. Kim, Invasive breast cancer: prognostic value of peritumoral edema identified at preoperative MR imaging, Radiology 287 (1) (2018) 68–75.
[6] H. Cheon, H.J. Kim, S.M. Lee, S.H. Cho, K.M. Shin, G.C. Kim, J.Y. Park, W.H. Kim, Preoperative MRI features associated with lymphovascular invasion in node-negative invasive breast cancer: a propensity-matched analysis, J. Magn. Reson. Imag. 46 (4) (2017) 1037–1044.
[7] B.B. Choi, Dynamic contrast enhanced-MRI and diffusion-weighted image as predictors of lymphovascular invasion in node-negative invasive breast cancer, World J. Surg. Oncol. 19 (1) (2021) 76.

[8] T. Igarashi, H. Furube, H. Ashida, H. Ojiri, Breast MRI for prediction of lymphovascular invasion in breast cancer patients with clinically negative axillary lymph nodes, Eur. J. Radiol. 107 (2018) 111–118.
[9] A. Conti, A. Duggento, I. Indovina, M. Guerrisi, N. Toschi, Radiomics in breast cancer classification and prediction, Semin. Cancer Biol. 72 (2021) 238–250.
[10] B. Feng, Z. Liu, Y. Liu, Y. Chen, H. Zhou, E. Cui, X. Li, X. Chen, R. Li, T. Yu, L. Zhang, W. Long, Predicting lymphovascular invasion in clinically node-negative breast cancer detected by abbreviated magnetic resonance imaging: transfer learning vs. radiomics, Front. Oncol. 12 (2022), 890659.
[11] Z. Liu, B. Feng, C. Li, Y. Chen, Q. Chen, X. Li, J. Guan, X. Chen, E. Cui, R. Li, Z. Li, W. Long, Preoperative prediction of lymphovascular invasion in invasive breast cancer with dynamic contrast-enhanced-MRI-based radiomics, J. Magn. Reson. Imag. 50 (3) (2019) 847–857.
[12] Q. Chen, J. Shao, T. Xue, H. Peng, M. Li, S. Duan, F. Feng, Intratumoral and peritumoral radiomics nomograms for the preoperative prediction of lymphovascular invasion and overall survival in non-small cell lung cancer, Eur. Radiol. 33 (2) (2022) 947–958.
[13] J. Zhang, G. Wang, J. Ren, Z. Yang, D. Li, Y. Cui, X. Yang, Multiparametric MRI-based radiomics nomogram for preoperative prediction of lymphovascular invasion and clinical outcomes in patients with breast invasive ductal carcinoma, Eur. Radiol. 32 (6) (2022) 4079–4089.
[14] C. Parmar, P. Grossmann, J. Bussink, P. Lambin, H.J.W.L. Aerts, Machine learning methods for quantitative radiomic biomarkers, Sci. Rep. 5 (1) (2015), 13087.
[15] A. Fedorov, R. Beichel, J. Kalpathy-Cramer, J. Finet, J.-C. Fillion-Robin, S. Pujol, C. Bauer, D. Jennings, F. Fennessy, M. Sonka, J. Buatti, S. Aylward, J.V. Miller, S. Pieper, R. Kikinis, 3d slicer as an image computing platform for the quantitative imaging network, Magn. Reson. Imaging 30 (9) (2012) 1323–1341.
[16] J.J. van Griethuysen, A. Fedorov, C. Parmar, A. Hosny, N. Aucoin, V. Narayan, R.G. Beets-Tan, J.-C. Fillion-Robin, S. Pieper, H.J. Aerts, Computational radiomics system to decode the radiographic phenotype, Cancer Res. 77 (21) (2017) e104–e107.
[17] T.L. Harada, T. Uematsu, K. Nakashima, T. Kawabata, S. Nishimura, K. Takahashi, Y. Tadokoro, T. Hayashi, K. Tsuchiya, J. Watanabe, T. Sugino, Evaluation of breast edema findings at t2-weighted breast MRI is useful for diagnosing occult inflammatory breast cancer and can predict prognosis after neoadjuvant chemotherapy, Radiology 299 (1) (2021) 53–62.
[18] N.J.-Y. Park, J.Y. Jeong, J.Y. Park, H.J. Kim, C.S. Park, J. Lee, H.Y. Park, J.H. Jung, W.W. Kim, Y.S. Chae, S.J. Lee, W.H. Kim, Peritumoral edema in breast cancer at preoperative MRI: an interpretative study with histopathological review toward understanding tumor microenvironment, Sci. Rep. 11 (1) (2021), 12992.
[19] H. Koyama, N. Kobayashi, M. Harada, M. Takeoka, Y. Kawai, K. Sano, M. Fujimori, J. Amano, T. Ohhashi, R. Kannagi, K. Kimata, S. Taniguchi, N. Itano, Significance of tumor-associated stroma in promotion of intratumoral lymphangiogenesis, Am. J. Pathol. 172 (1) (2008) 179–193.
[20] H. jae Lee, J.E. Lee, W.G. Jeong, S.Y. Ki, M.H. Park, J.S. Lee, Y.K. Nah, H.S. Lim, HER2-positive breast cancer: association of MRI and clinicopathologic features with tumor-infiltrating lymphocytes, Am. J. Roentgenol. 218 (2) (2022) 258–269.
[21] B.J. Kang, J.A. Lipson, K.R. Planey, S. Zackrisson, D.M. Ikeda, J. Kao, S. Pal, C.J. Moran, B.L. Daniel, Rim sign in breast lesions on diffusion-weighted magnetic resonance imaging: diagnostic accuracy and clinical usefulness, J. Magn. Reson. Imag. 41 (3) (2014) 616–623.
[22] Y. Choi, S.H. Kim, I.K. Youn, B.J. Kang, W. chan Park, A. Lee, Rim sign and histogram analysis of apparent diffusion coefficient values on diffusion-weighted MRI in triple-negative breast cancer: comparison with ER-positive subtype, PLoS One 12 (5) (2017), e0177903.
[23] H.D. Lee, K.H. Nam, C.M. Shin, H.S. Lee, Y.H. Chang, H. Yoon, Y.S. Park, N. Kim, D.H. Lee, S.-H. Ahn, H.-H. Kim, Development and Validation of Models to Predict Lymph Node Metastasis in Early Gastric Cancer Using Logistic Regression and Gradient Boosting Machine Methods, Cancer Res. Treat., 2023.
[24] C. Zhou, Y. Wang, M.-H. Ji, J. Tong, J.-J. Yang, H. Xia, Predicting peritoneal metastasis of gastric cancer patients based on machine learning, Cancer Control 27 (1) (2020), 107327482096890.
[25] W. Jiang, R. Meng, Y. Cheng, H. Wang, T. Han, N. Qu, T. Yu, Y. Hou, S. Xu, Intra- and peritumoral based radiomics for assessment of lymphovascular invasion in invasive breast cancer, J. Magn. Reson. Imag. (2023) 1–13.